drones

MDPI

Article

Using Digital Surface Models from UAS Imagery of Fire Damaged *Sphagnum* Peatlands for Monitoring and Hydrological Restoration

Shannon de Roos [1,*] , **Darren Turner** [2] , **Arko Lucieer** [2] **and David M. J. S. Bowman** [3]

[1]   Physical Geography, Faculty of Geosciences, Utrecht University, 3584 CB Utrecht, The Netherlands
[2]   Geography and Spatial Sciences, College of Sciences and Engineering, University of Tasmania, Hobart, TAS 7001, Australia; Darren.Turner@utas.edu.au (D.T.); Arko.Lucieer@utas.edu.au (A.L.)
[3]   School of Natural Sciences, College of Sciences and Engineering, University of Tasmania, Hobart, TAS 7001, Australia; David.Bowman@utas.edu.au
*   Correspondence: s.deroos@uu.nl; Tel.: +31644615543

check for **updates**

Abstract: The sub-alpine and alpine *Sphagnum* peatlands in Australia are geographically constrained to poorly drained areas c. 1000 m a.s.l. *Sphagnum* is an important contributor to the resilience of peatlands; however, it is also very sensitive to fire and often shows slow recovery after being damaged. Recovery is largely dependent on a sufficient water supply and impeded drainage. Monitoring the fragmented areas of Australia's peatlands can be achieved by capturing ultra-high spatial resolution imagery from an unmanned aerial systems (UAS). High resolution digital surface models (DSMs) can be created from UAS imagery, from which hydrological models can be derived to monitor hydrological changes and assist with rehabilitation of damaged peatlands. One of the constraints of the use of UAS is the intensive fieldwork required. The need to distribute ground control points (GCPs) adds to fieldwork complexity. GCPs are often used for georeferencing of the UAS imagery, as well as for removal of artificial tilting and doming of the photogrammetric model created by camera distortions. In this study, Tasmania's northern peatlands were mapped to test the viability of creating hydrological models. The case study was further used to test three different GCP scenarios to assess the effect on DSM quality. From the five scenarios, three required the use of all (16–20) GCPs to create accurate DSMs, whereas the two other sites provided accurate DSMs when only using four GCPs. Hydrological maps produced with the TauDEM tools software package showed high visual accuracy and a good potential for rehabilitation guidance, when using ground-controlled DSMs.

Keywords: UAS; GCP; DSM; *Sphagnum*; peatlands; TauDEM; restoration

1. Introduction

The Earth's peatlands are experiencing widespread environmental pressures, caused by climate change as well as anthropogenic forces. Some of the main dangers include increased frequency and severity of droughts, a higher wild fire frequency, drainage, and peat mining [1–3]. Another threat to the peatlands in Australia is created by the trampling and grazing of feral animals, which results in compaction and drainage and eventual desiccation of peatlands [1,4]. Little is known about the response of peatlands to these disturbances [2,5]. Yet peatland ecosystems play a vital role in local and global environmental processes.

Peatlands are wetlands with a low mineral content (<35%) and an organic soil layer of at least 30 cm depth [6,7]. This organic layer is sustained by a high-water table which creates anaerobic conditions and maintains a low decomposition rate. These conditions make peatlands a major global carbon sink: covering barely 3% of the Earth's surface, boreal and subarctic peatlands function as a sink

for 15–30% of the global soil carbon, resulting in a net cooling effect on the Earth's climate [6–8]. Apart from their global climatic importance, peatlands fulfill a hydrological function in catchments, acting as water flow regulators. With an exceptionally high water holding capacity, peatlands efficiently store surface water, thereby filtering out sediment and moderating runoff [1,9].

In Australia, 0.14% of the total land mass is covered by peatlands [10]. This includes coastal peatlands and peatlands in the sub-alpine and alpine regions of south eastern Australia that occur c. 1000 m Above Sea Level (a.s.l.) [11]. The sub-alpine or alpine peatlands are either montane mires or *Sphagnum* dominated communities, geographically constrained to poorly drained areas and therefore at risk of ecological collapse [1,11].

Sphagnum, a large colonial bryophyte, is considered to be an important contributor to the resilience of sub-alpine and alpine peatlands, as it can easily survive under extremely nutrient-poor conditions and can produce resistant organic matter which further promotes peat accumulation [1,8,12]. *Sphagnum* mires are also an important habitat for several wildlife species including endangered frogs, such as the Corroboree frog [10]. In Tasmania on the Central Plateau, *Sphagnum* often forms the understory of the endemic conifer pencil pine (*Athrotaxis cupressoides*). Pencil pines are endemic to Tasmania and are mainly concentrated on the broad Central Plateau, where they develop on open sites [13,14]. They are a long-lived species, growing up to 1000 years in age and contain seed productions of 5–6 year intervals. The first seed production generally sets in after the pencil pine has reached an age of 100 years [13,15].

There are numerous records of peatland damage from wildfires in Australia that result in the loss of peat soils and modify their drainage [16–18]. Both *Sphagnum* and pencil pine are known to be fire sensitive species (Figure 1). Post-fire conditions of *Sphagnum* bogs often show slow recovery, or conversion into grass and fern dominated lands [18–20]. Pencil Pine are very sensitive to fire, grow slow and episodically produce seed and typically reproduce colonially [21]. Because of these properties, pencil pine is rarely found to be naturally recovering after fire damage and has undergone a range of declines through the Holocene, and particularly since European colonization 200 years ago [21,22].

(a)   (b)

Figure 1. (**a**) Healthy *sphagnum* from Skullbone Plains, near Bronte Park, Central Tasmania; (**b**) Post-fire conditions of burnt *Sphagnum* and pencil pine trees near Lake Mackenzie, Northern Tasmania.

Two examples of severe peat fires in the last century are the 1961 fire in the Tasmanian Central Plateau and the 2003 fire in the Australian Alps, Victoria. The Tasmanian fire of 1961 was human-ignited and over a period of five months it smoldered in approximately 60% of the Tasmanian Central Plateau, reducing 20,000 ha of peat soils into mineral soils [13,17]. The Victorian 2003 fire was preceded by three years of drought, leaving the peatlands in the Alps dehydrated and susceptible to fire [16]. As a result, almost all the alpine, subalpine and montane mires and fens in Victoria were burnt, causing a loss of approximately 15% of the functional plant communities [16].

Clarkson et al. [10] stated that the relatively small peatland extent of Australia and low levels of research funding have contributed to limited peatland restoration programs and research publications.

However, with *Sphagnum* as the dominant contributor to continuing accumulation of organic matter in peatlands, recovery of *Sphagnum* is essential for subalpine and alpine peatland communities [16]. In Tasmania, rehabilitation of *Sphagnum* has never been extensively trialed, thus, post-fire peatland management is of increasing importance here [19].

To make peatland rehabilitation methods more efficient and effective, an improved knowledge of the response of peatlands to disturbances is required [1,7,22]. Current physical mapping and monitoring techniques of Australia's peatlands, such as described by Whinam et al. [18] and Clarke and Martin [23], are often labor intensive, time consuming, and can further damage peatlands by stepping on this delicate vegetation. Additionally, the use of sample areas (quadrats and transects) generally covers only 1–4% of the peatland being studied, hence, are vulnerable to sampling bias. Alternatively, conventional remote sensing techniques such as satellites and aerial photography are inefficient for peatland monitoring due to the fragmented nature and typically small areas (<1–2 ha) of individual peatlands in Australia [11]. Moreover, to capture the detailed information of peatlands such as species composition and vegetation health, sub decimetre resolution imagery is required, which traditional remote sensing techniques cannot provide. Ultrahigh spatial resolution (<10 cm/pixel) images are also required to capture the micro-topography of peatlands, which is essential for the monitoring of hydrological pathways and peat bog volumes.

Surveying the fragmented areas of Australia's peatlands can be achieved by capturing ultra-high spatial resolution imagery from unmanned aerial systems (UAS, UAVs, or drones). A small UAS is ideal for mapping areas of <10 ha with an ultra-high resolution where 1–2 cm/pixel is feasible for the typical areas that *Sphagnum* mires cover. Also, UAS have previously proven their suitability for environmental mapping and monitoring of micro-topography and species composition including moss beds [24–26]. To map and monitor *Sphagnum* mires over a larger geographical area that contains hundreds of individual mires, it would be necessary to select a representative sample of *Sphagnum* mires. The spectral information provided by the high-resolution images from a UAS, has the potential to provide a better insight into different health states of the *Sphagnum* moss. Additionally, digital surface models (DSMs) can be created by generating very high-resolution 3D point clouds with photogrammetric software and computer vision techniques. High resolution DSMs, can be used for hydrological modelling to provide detailed information about flow directions of surface water and suitable locations for rehabilitation methods within each *Sphagnum* mire, such as channel blocking [10].

Images captured by a UAS are typically geotagged with the camera location at the time of image capture, the position being supplied by the onboard global navigation satellite system (GNSS). However, with a potential error of several meters, these positions do not have a geometric accuracy that is compatible with the ultra-high resolution UAS imagery [26]. Furthermore, DSMs generated from UAS imagery with low accuracy geotagging and lack of high accuracy ground control can be artificially tilted or have a more complex form of geometric distortions, such as doming or twisting, resulting in inaccurate hydrological models. To create a reliable DSM, a more accurate method of image georeferencing is required. A commonly applied method to remove these distortions is the use of ground control points (GCPs). The markers are laid out in the mapped area and their geographic coordinates are measured using a differential GPS (DGPS) real time kinematic (RTK) system with an accuracy of approximately 2 cm in the horizontal and 4 cm in the vertical directions. The markers are later manually identified in the images and used during structure from motion (SfM) and multiview stereopsis (MVS) algorithms. This enhancement of the photogrammetric model accuracy corrects many model distortions and translates the model into an accurate real-world co-ordinate frame. However, the use of GCPs during fieldwork is time-consuming and labor intensive, especially for areas that are not easy to access [27]. Furthermore, for vulnerable areas such as peatlands, manual placement, and retrieval of GCPs can damage the delicate vegetation within the study site. Minimizing the amount of GCPs will minimize the amount of damage caused by trampling.

A few studies have documented the distribution of GCPs in relation to DSM accuracy [28–30]. Harwin et al. [29] found that accuracy mostly decreased in vertical direction when reducing the

amount of GCPs, and highlighted the importance of precise control. Gindraux et al. [30] stated that DSM accuracy is further influenced by factors such as camera focal length, flying height, and image quality. Along with varying sizes and complexity of the topography of study areas, comparisons between studies are difficult to make. Tonkin and Midgley [28] came to the conclusion that for an area of irregular topography, the use of four or more GCPs is acceptable, with a vertical RMSE of 0.064 m, compared to a vertical RMSE of 0.059 with 101 GCPs. The spatial distribution of the GCPs was highlighted, where vertical errors increased significantly after 100 m distance between GCPs with a flight altitude of 280–330 m above sea level (ASL).

The objective of this study is to test the viability of hydrological modelling of peatlands covering approximately 1 ha and to determine the amount of GCPs that are required to create reliable DSMs.

2. Materials and Methods

2.1. Study Area

On 13 January 2016, a dry lightning storm ignited more than 80 bushfires across western Tasmania [19]. The ignition points at Dove River, February Plains, Lake Bill, and the Mersey Forests combined to form the Mersey Forest Fire Complex, burning an area of ~25,000 ha over a period of approximately three months (Figure 2). Prior weather conditions, a cold and dry winter followed by a dry and warm spring, were a critical factor for this event to occur. The final trigger was the absence of significant rainfall leading up to the event. The fire was largely under control by February, however peat soils continued to burn until early May [19]. Approximately 85 ha of Pencil Pine (*Athrotaxis cupressoides*) woodland were present in the burnt area, which is a little over 1% of the currently mapped distribution in Tasmania [19]. Due to their fire sensitive nature, it was expected that there would be a high rate of mortality amongst the Pencil Pines. Mapping of *Sphagnum* mires after the fire indicates that there are upwards of 200 individual patches of *Sphagnum* totaling approximately 40 ha, which is merely a small fraction of the total plateau area. However, the extent of *Sphagnum* peatlands in the burnt area is estimated to be approximately 1% of the nationwide coverage. Observations made after the fire estimated that 71% of the surveyed *Sphagnum* sites were burnt to the point of significant damage.

Field campaigns for this study were carried out in late 2017, from 21 to 23 November and from 7 to 10 December. During these visits, five different sites of *Sphagnum* dominated peatland communities were mapped on the Central Plateau, within the fire boundary of the Mersey Forest Fire Complex (Figure 2). The area of the mapped sites are typically around 1 ha and their altitude ranges between 1120 m and 1260 m above mean sea level (AMSL). Study sites were named based on local features and their topographic characteristics. The sites Eagle Valley (EV), Basin (BN), and Flat Valley (FV) are rectangle-shaped basins surrounded by rocky ridges, where surface water easily collects in pools. All three sites contain several patches of burnt Pencil Pine trees, which are the most abundant in Eagle Valley. The Jack's Lagoon (JL) site consists of a *Sphagnum* dominated community and is almost absent of Pencil Pines. It comprises the largest area and the highest altitude of all sites. The most northern area, named Heath (HT), consists of *Sphagnum* mires situated on a gently easterly sloping area.
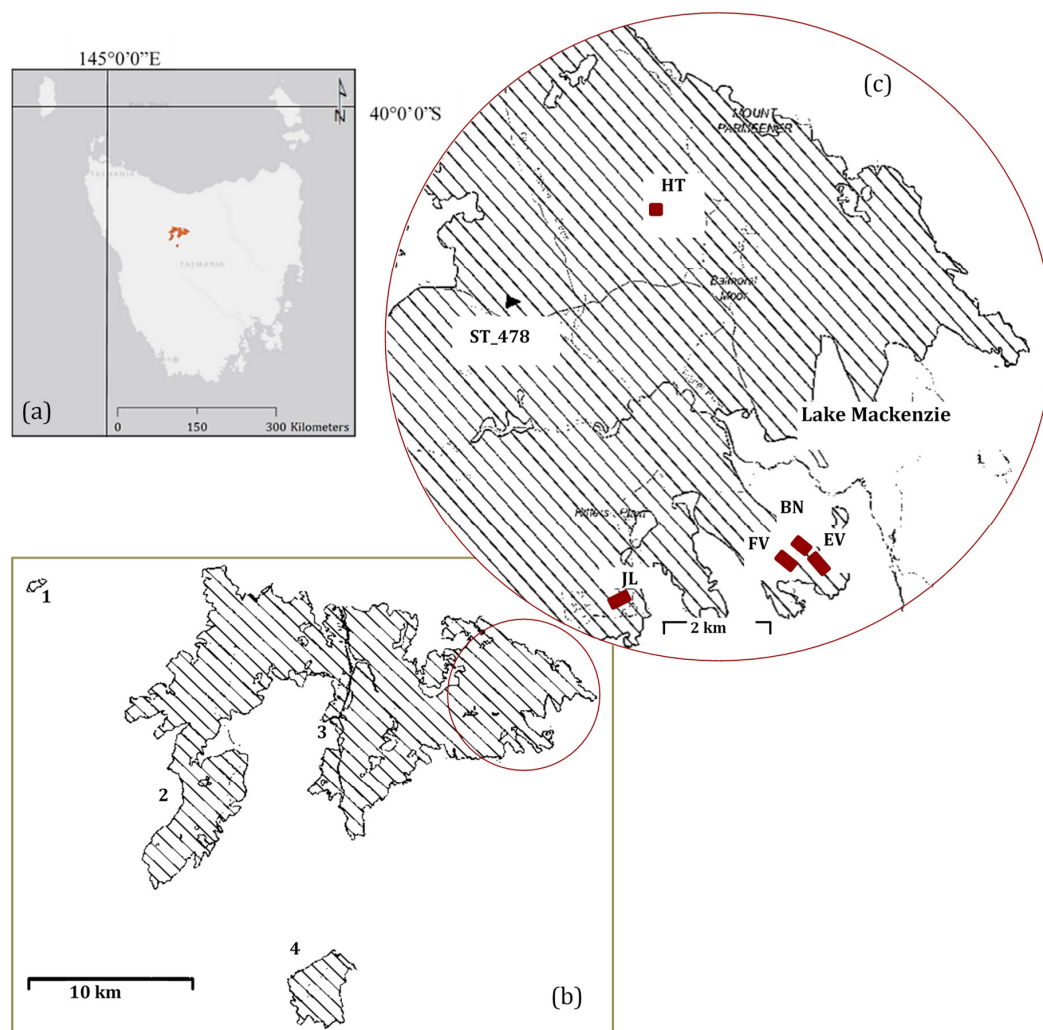
Figure 2. (**a**) Fire boundary of the Mersey Fire Complex (2016) in Tasmania; (**b**) Ignition points at **1**. Dove River, **2**. February Plains, **3**. Mersey Forests, **4**. Lake Bill; (**c**) Locations of the study sites are shown and the location of the RTK DGPS Base station, placed on marker ST_478.

2.2. UAS Platform

A DJI Phantom 4 Pro (DJI, Shenzhen; https://www.dji.com/phantom-4-pro) was used to map all five sites in the study area. The DJI Phantom is equipped with a CMOS active pixel sensor camera, which is mounted on a gimbal to stabilize it during the flight. The camera collects 20-megapixel imagery at a rate of one image every two seconds. The DJI Phantom contains a navigation-grade global navigation satellite system (GNSS) receiver that is used by the autopilot to follow a predefined flight plan and to geotag the imagery captured during flight. For each site, the positions of the four corner GCPs were marked and stored in the ground control software, Ground Station Pro (GS Pro), to help delineate the flight boundaries. This allowed GS Pro to automatically calculate a flight pattern consisting of a series of way-points that would provide coverage of the site at the desired overlap settings. Two grids were flown at the same elevation above the ground (Figure 3a,b), these two grids were then combined to create what is referred to as a double grid (Figure 3c). Flying heights varied between sites depending on spatial extent, but commonly started at 30 m above ground level (AGL). For UAS mapping of 3D structure, high overlaps (>70%) are required [31], and this for this study we used a forward image overlap of 80% and a side overlap of 75%. Flight details of each site can be found in Table 1. This table also includes the ground sample distance (GSD) and the altitude range. Because

the *Sphagnum* mires develop on generally flat areas, the effect of GSD is not significant for this study and the main variations in altitude are caused by the rocky edges at the borders of the study sites.
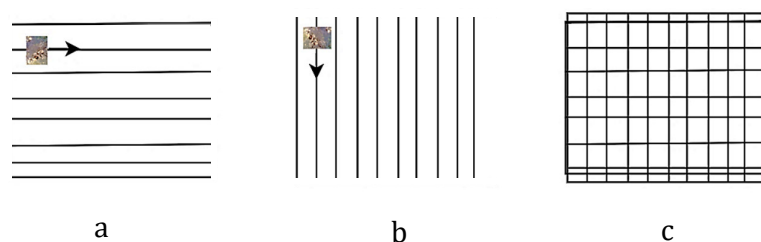

a   b   c

Figure 3. Different flight patterns used for each site at lowest altitude with (**a**) a single grid (Grid 1), (**b**) a second single grid (Grid 2), and (**c**) a double grid consisting of patterns a and b combined.

Table 1. Details about each study site including the number of photos acquired by DJI Phantom and the ground sample distance (GSD) of the orthophotos and digital surface models.

		Jack's Lagoon (JL)	Eagle Valley (EV)	Flat Valley (FV)	Basin (BN)	Heath (HT)
Area (m^2)		10,280	7044	3805	5250	4928
Altitude range ASL (m)		1258–1266	1202–1206	1206–1222	1177–1201	1119–1141
Flying height AGL (m)		40	30	30	30	30
Number of Images	*Grid 1*	364	243	140	274	134
	Grid 2	357	271	160	292	169
	Double Grid	721	514	300	566	303
GSD (cm)	*Orthophoto*	2	1	1	1	2
	DSM	3	2	2	2	3

2.3. Georeferencing

The markers that served as GCPs for this study were made of laminated A3 size sheets of paper and contained a black dot indicating the center. The markers were kept in place on the ground with metal pegs. For each site, four control points were laid out at the corners, after which a remaining 12 to 16 markers were distributed randomly over the study area such that they were evenly distributed within the rectangle formed by the corner points. There was not method used for this, it was simply based on years of experience in GCP distribution (see Figure 4). The 3D geometric positions of the GCPs were measured with accuracies of 2–4 cm in horizontal and 4–8 cm in vertical directions with a real-time kinematic dual frequency Leica 1200 DGPS system (Leica Geosystems, Heerbrugg, Switzerland). The receiving antenna (the rover) was held by the operator on the marker (with the assistance of a tripod to keep the antenna level) whilst receiving corrections from a local base station, situated within 6.2 km radius (see ST_478 marker in Figure 2c).

The photogrammetry software, Agisoft Photoscan (Agisoft, Saint Petersburg, Russia) Professional version 1.4.1, was used to generate 3D models from the photographs. Photoscan utilizes modern structure from motion (SfM) and multiview stereopsis (MVS) algorithms to process multiple UAS images and thus enables the creation of an orthophoto and DSM of the area over which imagery was captured. Detailed descriptions of typical Photoscan workflows can be found in Verhoeven [32]. In a typical workflow, GPS coordinates from the cameras are used to identify the 3D position of each keypoint and a sparse point cloud of the area is created. The image alignment was initially executed in Photoscan using a low accuracy to arrange the images into an approximated position to assist with the identification of GCPs. Manual georeferencing was applied by identifying the GCPs in as many images as possible, after which camera calibration parameters (f, cx, cy, k1-k4, b1, b2, p1, p2) were optimized and all images were re-aligned using a high accuracy setting. The alignment in high accuracy was run with no restriction on the maximum number of keypoints and tie points. The second phase, MVS, searches for additional points and densifies the point cloud, which in this study resulted in an increase in the number of points by an approximate factor of 10. For the point cloud densification in Photoscan,

quality was set to high and depth filtering was kept at default (aggressive) as it was found that this option filters out the anomalies, hence creates smoother and more reliable surfaces for open sites.

Three scenarios were created and applied to each site (see Figure 4). For one of the scenarios, only the approximate GPS locations of the cameras (geotags) were used to generate a DSM and orthophoto. This scenario is referred to as Sky_GCP. In the second scenario, Four_GCP, only the four GCPs located in the corners of the site were used for georeferencing. The third scenario uses all GCPs (16–20) for model georeferencing and is referred to as All_GCP. Models that have not been controlled with accurate position data can often contain distortions, which are normally corrected via the use of accurate GCPs. The DSM based on the model that used all GCPs was used as the reference scenario as it was the most accurate and robust DSM for each site. For the Sky_GCP scenario, where no manual GCP identification was applied, the image matching phase was directly executed in high accuracy.
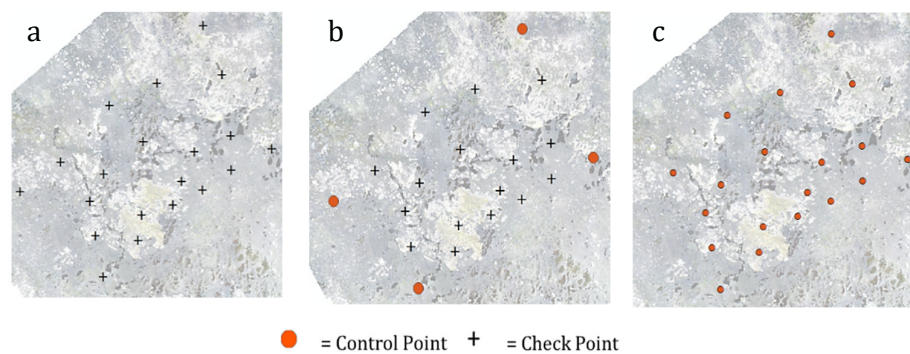

● = Control Point　　+ = Check Point

Figure 4. The three scenario's (**a**) Sky_GCP, (**b**) Four_GCP, and (**c**) All_GCP for the study site Flat Valley. The figure simultaneously gives an indication of the distribution of the GCPs.

2.4. Accuracy Assessment

Two different approaches were used to analyze the DSM accuracy. First, the vertical error of each DSM was quantified by using the GCPs as checkpoints. For each site, the DSMs and orthophotos of the different scenarios were exported from Photoscan. The orthophotos were required to visually assess the locations of the GCP markers. For the SKY_GCP scenarios, all GCPs could be used as checkpoints to calculate the root mean square error (RMSE) and standard deviation (STDEV) of the absolute error. For the Four_GCP scenarios, all but the corner GCPs were used as checkpoints. For the third scenario, All_GCP, no checkpoints were available as all points were used as GCPs (see Figure 4). The vertical errors of these points provided by Photoscan were used to obtain the RMSE and STDEV. This does not provide a true accuracy assessment, but rather the residuals of the process to fit the point cloud model to the GCPs. However, these values were necessary as a comparison to analyze the performance of the other two scenarios. Additionally, it could give an indication of the internal precision of the GCP based DSMs which were used as the reference scenario for later stages of our analysis.

The second accuracy assessment technique quantified the amount of artificial slope (i.e., slope that was not present in the real world) that could be found in the poorly controlled DSMs. The DSM from each scenario was compared to the reference DSM, which was assumed to be corrected from any tilting and sloping effects since all the GCPs were used to control the photogrammetric model. The first step of the slope analysis was to shift the planimetric location of the SKY_GCP DSMs to the same location as the reference GCP controlled DSM. This was done by identifying and matching the center of five GCPs from the respective orthophotos and using ENVI 5.4 (Harris Geospatial, Broomfield, CO, USA; https://www.harris.com/solution/envi) to apply a polynomial transformation with nearest neighbor resampling. The Four_GCP based DSMs did not require this transformation as the use of the four corner GCPs meant that they were already in the same planimetric location as the reference DSMs. Once alignment was complete, the SKY_GCP and Four_GCP scenarios were then subtracted from the reference DSM, which resulted in a difference map. Transects were then extracted at all angels

of the compass (i.e., 0°–360° at 1° steps) from the difference map. The slopes of these transects were calculated, and the maximum tilt of the DSM could then be identified from the set of extracted transects.

2.5. Hydrological Surface Models

The primary objective of this study was to create reliable DSMs of *Sphagnum* peatlands such that they could be used to create hydrological surface models. Broad-scale hydrological modelling algorithms are designed for large catchments (>100 km^2) and are generally not suitable for microtopography surface models with a high spatial resolution. This study implemented a similar hydrological modelling technique that was used by Lucieer et al. [33] to simulate snowmelt runoff in Antarctic moss beds. The *Sphagnum* peatlands have a similarly complex microtopography to the Antarctic moss beds thus it was hypothesized the same hydrological modelling process would be suitable. This technique makes use of the TauDEM command-line tools (Utah State University, Logan, UT, USA) [34] and requires a DSM as input to allow simulation of water flow and surface wetness. TauDEM uses the D-infinity contributing area algorithm to compute the relative flow accumulation. The D-infinity algorithm is an adaption to the D-8 algorithm, which assigns the value of the center grid cell to one of its eight neighboring cells with the steepest slope [35]. The D-infinity approach uses a continuous angle to calculate the direction of flow, providing more possibilities for flow directions and thus a more realistic model [34]. For detailed information about the TauDEM tools, see Tarboton and Mohammed [36].

The hydrological model was applied to the Heath study site, as during the accuracy assessment this site was found to have low vertical errors. The reference DSM, the Four_GCP and Sky_GCP scenario DSMs were used for hydrological modelling testing and comparison. This was repeated for an additional site, Basin, which showed a lower DSM accuracy compared to the Heath site. The pencil pine trees needed to be removed from the DSM prior to hydrological modelling, which was done using the Photoscan "classify ground points" algorithm with default settings (max. angle 15 degrees, max. distance 1 m and cell size 50 m). Otherwise, the pencil pines could add an extra uncertainty to the eventual hydrological models. Additionally, a Monte Carlo simulation was applied to each DSM, to account for the relative vertical error in the model. The Monte Carlo simulation created slightly different realizations of the DSM, by adding a predefined amount of random noise to the height values of the DSM. The range of noise is defined by the standard deviation of the error derived from GCP validation of the DSM. In this study we used the same value for random noise (0.044 m) as found by Lucieer [33] as this is a typical value when conducting an RTK based ground controlled UAS survey. The outputs of 150 DSM derivatives were used as inputs for the hydrological model. To improve the speed of the DSM error computations, the spatial resolution of the DSMs was reduced from 2 to 10 cm. The simulation of the reference DSM was run in full resolution as well, showing no obvious visual difference in the final output.

The Monte Carlo simulation was implemented in Python and was used to run three TauDEM command line tools for each DSM iteration: pitremove (removal of pits), dinfflowdir (D-infinity flow directions), areadinf (D-infinity contribution area or flow accumulation). The outputs of these three steps were then used to calculate a topographic wetness index (TWI), which is described by the inverse relation between the contributing area and the slope [37].

3. Results

3.1. DSM Accuracy Assessment

The absolute accuracy and artificial slopes for each scenario were analyzed and the results are shown in Table 2. From the five study sites, the sites Heath and Jack's lagoon performed best for both the error assessment and slope analysis. The vertical errors of the Four_GCP scenarios for both Heath and Jack's Lagoon remained almost equal to the GCP scenarios. For both these sites an artificial slope was evident in the Four_GCP DSMs, but did not exceed 0.05 degrees. For the other sites (BN,

EV, FV), DSM vertical errors significantly increased in the Four_GCP DSM scenarios. For Flat Valley, an artificial slope of 0.1 degrees was found for the same scenario. For Basin and Eagle Valley, the DSM difference map showed doming effects instead of slopes and due to an extreme amount of noise in the point clouds used to generate the DSMs, no maximum slope could be determined. Comparing the Four_GCP scenarios to the Sky_GCP scenarios, a significant improvement is visible in both the vertical error and sloping effects for all sites (Table 2). For the Sky_GCP scenarios, sloping effects exceeded 1 degree for BN, EV, and FV, but remained below 1.0 degrees for HT and JL.

In addition to the shown scenarios, more scenarios for each site were created using imagery from one or two additional flying heights consisting of single grids, with the aim to make the photogrammetric model alignment more robust especially in terms of topography. However, no (significant) improvement of using multiple flying heights could be found for any of the scenarios, whilst processing time increased exponentially as extra flying heights were introduced. The All_GCP scenarios from multiple flying heights did indicate that the reference scenario (All_GCP) remained relatively stable, as no artificial slopes became apparent during subtraction of DSMs.

Table 2. Results of DSM accuracy assessment, showing the root mean square error (RMSE) of the DSM in vertical direction, measured with vertical GCP values as reference, the standard deviation (STDEV) of the absolute errors and maximum slope measured from the DSM difference maps for each scenario, for the five study sites. Note that the values of the All_GCP scenarios are solely based on the vertical errors provided by Photoscan, as no checkpoints were available.

		All_GCP	Four_GCP	Sky_GCP
Basin—BN	RMSE (m)	0.03	0.58	0.28
	STDEV (ABS error)	0.02	0.41	0.32
	Max slope (°)	0.00	domed	1.50
Eagle Valley—EV	RMSE (m)	0.03	0.83	1.20
	STDEV (ABS error)	0.03	0.33	0.45
	Max slope (°)	0.00	domed	1.25
Flat Valley—FV	RMSE (m)	0.09	0.19	0.73
	STDEV (ABS error)	0.04	0.07	0.35
	Max slope (°)	0.00	0.10	1.10
Heath—HT	RMSE (m)	0.02	0.03	0.21
	STDEV (ABS error)	0.01	0.02	0.14
	Max slope (°)	0.00	0.05	0.35
Jack's Lagoon—JL	RMSE (m)	0.02	0.02	0.31
	STDEV (ABS error)	0.01	0.01	0.19
	Max slope (°)	0.00	0.04	0.75

3.2. Hydrological Surface Model Assessment

The Heath study site was used to assess the quality of the hydrological surface models from the three main scenarios. Figure 5 displays the orthophoto and DSM of the site and the two end products of the hydrological modeling process (Section 2.5) derived from the reference DSM. These are the average flow accumulation and topographic wetness index, averaged from 150 iterations of the Monte Carlo simulation. The damaged *Sphagnum* mires are situated approximately in the center and are indicated in Figure 5a. The DSM clearly shows the natural slope in easterly direction, where the largest altitude difference is caused by the rocky ridge in the West. There is a maximum elevation difference of 22 m, which implies an average slope of approximately 6.5°.

The flow accumulation map shows the distribution of water accumulation over the study site. The streams indicated in the south eastern corner (Figure 5c-i) coincide with streams that were present at the study site and can also be seen in the orthophoto. The larger stream is fed from smaller streams northeast of the map, which coincide in the orthophoto with the location of a small pool complex (Figure 5a-ii). The streams formed on the western side most likely originate from accumulation caused

by the sloping edge in the northwestern part of the map. It can be further noticed that the major stream lines do not flow over the *Sphagnum*, although some of these channels gain their water partially from the smaller streams generated in the *Sphagnum* mires. The topographic wetness index map shows wet patches that overall, coincide well with the pools in the orthophoto (Figure 6). The pool complex in the northeast is however not well represented by the TWI map, as it shows smaller and fewer pools than were actually present (Figure 5a-ii,d). Additionally, several tiny wet patches are created in between the *Sphagnum* mires, which were not present during field survey. Overall, the *Sphagnum* is represented as relatively dry in the TWI map as well as in the flow accumulation map.

After processing the reference scenario, the hydrological models were run using the DSMs of the Four_GCP and Sky_GCP scenarios at one height. These DSMs contained a maximum artificial slope of 0.05° and 0.35° respectively compared to the reference scenario (Table 2). There were no significant visual differences found between the reference model outputs and Four_GCP and Sky_GCP scenarios. Small differences in streamlines can be seen in the flow accumulation map, however, the most significant streamlines were similar in all three scenarios. No visual differences were found between the TWI maps of the different scenarios.
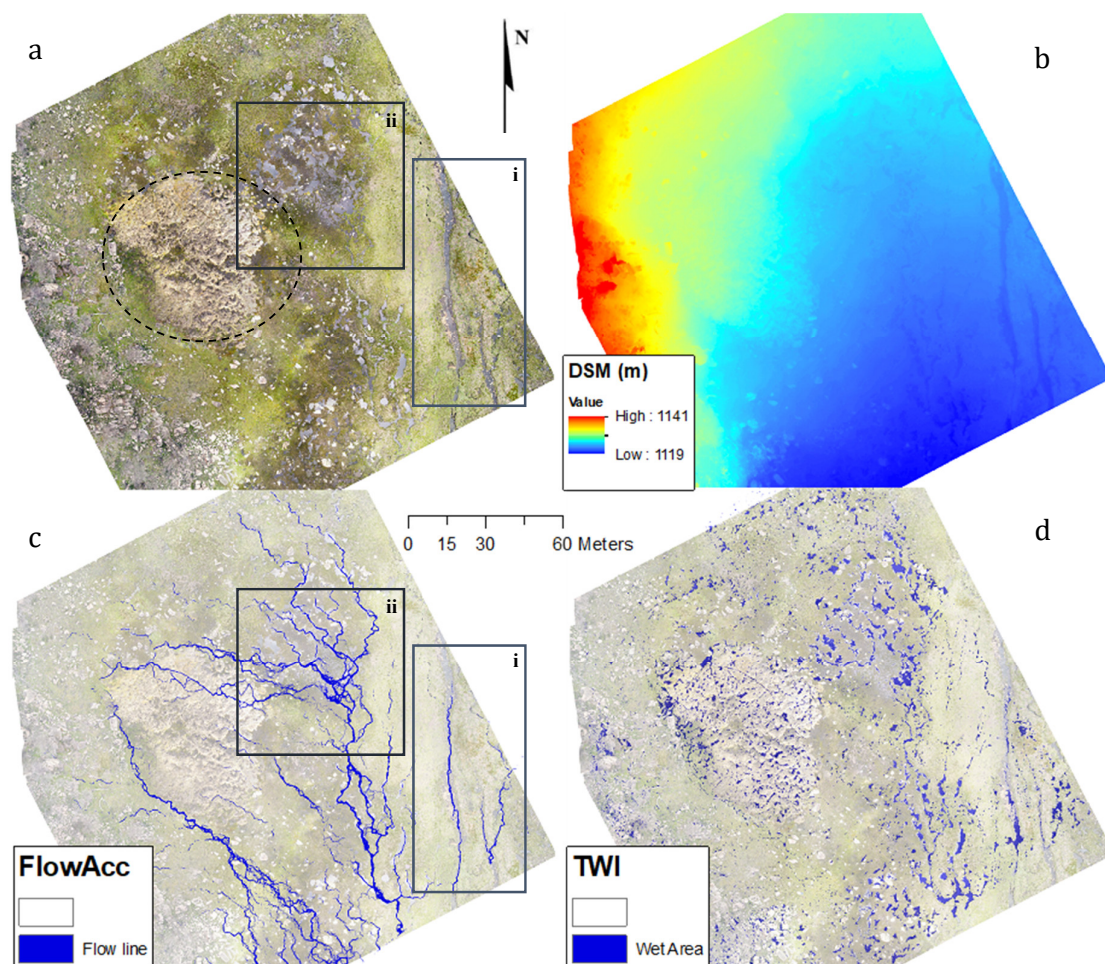

Figure 5. (**a**) Orthophoto of the Heath study site with a dashed circle indicating the position of *Sphagnum* peatlands; (**b**) DSM from the reference scenario; (**c**) flow accumulation model derived from reference DSM; and (**d**) topographic wetness index map derived from the reference DSM.
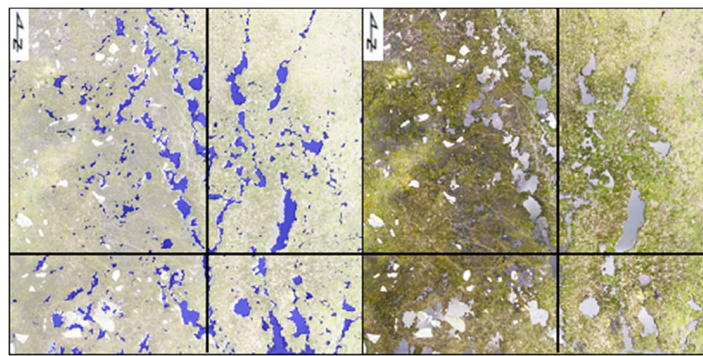
Figure 6. The left image shows a zoomed part southeast of the TWI index of Heath (All_GCP) and the right image shows the same part from the orthophoto. The size of the area is approximately 50 × 50 m.

The hydrological model process (Section 2.5) was repeated for the Basin study site, using the reference DSM and Sky_GCP DSM. The Basin site differs topographically from Heath as it is a relatively flat area, surrounded by steep rocky ridges, instead of sloping in one direction. During the accuracy assessment, the DSM subtraction of these two scenarios showed significantly larger artificial slopes than for the study site Heath. In Figure 7a, the DSM of the reference scenario is overlain on the orthophoto, showing the rocky ridges in the Southeast. The TWI maps of Sky_GCP and reference scenario can be seen in Figure 7b,c respectively and visual comparison demonstrates one major difference. Where the TWI map of the reference scenario captures the positions of the pools as is shown in the orthophoto, for the Sky_GCP scenario, a large pool was created right below the steep rocky ridges. This large feature was not present during field survey and is also not visible in the reference TWI map. The maximum artificial slope for Sky_GCP of 1.5° (see Table 2) is directed towards this pool (SE). There was no artificial doming created for this scenario.
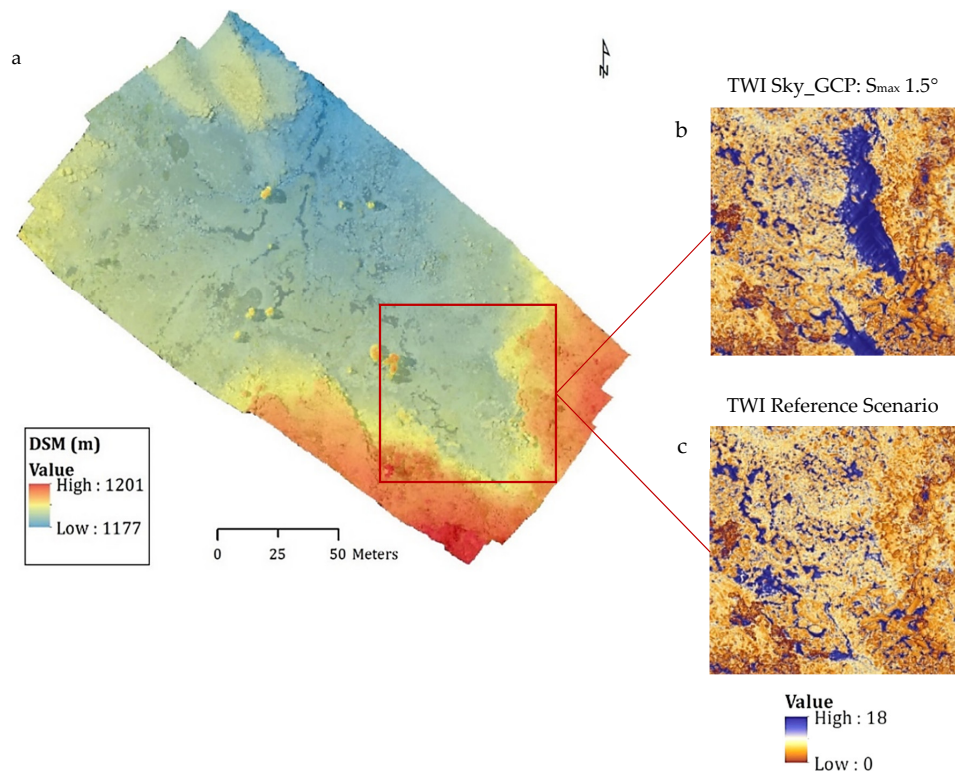

Figure 7. (**a**) DSM of the Basin reference scenario overlain on the orthophoto; (**b**) a zoomed part of the topographic wetness index map of Sky_GCP scenario; and (**c**) a zoomed part of the topographic wetness index map of the reference scenario.

4. Discussion

4.1. DSM Accuracy Assessment

Five different *Sphagnum* dominated study sites in northern Tasmania were surveyed with a UAS, and DSMs were generated using different georeferencing scenarios. Overall, the vertical errors that were computed by Photoscan for the All_GCP scenarios (16-20 GCPs) were similar to findings of other studies that used ground control for UAS derived DSMs and found to be in the range of ~0–5 cm [28,33,38–40]. For the Four_GCP scenarios, the errors remained similar to the All_GCP scenarios for the Heath and Jack's lagoon sites, but increased to exceed 10 cm for the remaining scenarios. Additionally, doming in the DSMs occurred in the Four_GCP scenarios for Eagle Valley and Basin. It should be noted that the topography of Eagle Valley was naturally doming (altitude was highest towards the center of the site), which could have been an underlying reason for the doming effect that occurred for Eagle Valley Four_GCP. As previously mentioned, Tonkin and Midgley [28] found errors below 10 cm when using four ground control points, whereas the study conducted by Clapuyt et al. [26] revealed larger errors when using four corner points, with a mean of 0.31m, compared to a mean of 0.02m when using 15 GCPs, for a similar sized area. Clapuyt et al. [26] came to the conclusion that georeferencing errors increase proportionally with distance between GCPs, resulting in larger errors and weak reproducibility with irregularly scattered GCPs. Additionally, James et al. [41] stated that control precision, i.e., the effect of underestimation or overestimation of control point accuracy, is equally important as the GCP distribution. Harwin and Lucieer [27] commented that variation in terrain should be considered with GCP distribution, where steeper terrain requires a higher GCP density.

A few hypotheses are presented that could explain the overall higher accuracy performance of Heath and Jack's Lagoon, compared to the other sites, Basin, Eagle Valley, and Flat Valley. First, the DSMs of Heath and Jack's lagoon differed from the other sites, as they were relatively square in shape, whereas the areas of the other sites were an elongated rectangle. Additionally, Basin, Eagle Valley, and Flat Valley were surrounded by steep terrain that was (partially) captured by the UAS and pencil pine trees were distributed over the area. These factors increased the amount of DSM variation in vertical direction and might have added a complexity factor to mapping the topography.

This study has highlighted that for reliable DSM production GCPs are required. Whilst using as few as four GCPs did produce accurate results for some trial sites, this method did not work in all cases (see Table 2) and thus cannot be used confidently. An alternate method for removing the need for GCPs was tested during this study. That is, for one site (Basin) we collected imagery on two separate field trips, under different lighting conditions (one late in the evening, one during the afternoon). The afternoon imagery contained GCPs and was processed and aligned based on camera reference with Photoscan to create an orthophoto and DSM. The late evening imagery was then imported into the Photoscan job and aligned with the already controlled afternoon imagery. The original afternoon images were then disabled, and the orthophoto and DSM created based on the now accurately aligned evening imagery.

The aim of this methodology was to effectively control the second image dataset based on the first, if this were successful it would mean that once there is an accurately controlled model of a site, subsequent image collections would not need control as they could be matched to the earlier dataset. This method requires the scenes to have sufficient elements that remain unchanged over time, such that features can be matched between the two datasets. It was hypothesized that this would work for the peatlands as they contain a lot of rocks that will not change over relatively short time frames.

The method of aligning new images to a controlled model was not successful. Whilst the orthophoto produced with this methodology had an accuracy of 1–2 pixels in comparison to the fully controlled orthophoto, there were issues with the DSM. The DSM exhibited a significant artificial slope (>1°) similar to the Sky_GCP scenarios (see Table 2). Thus, for the purposes of this study, which

relies on accurate DSMs for hydrological surface modelling, this method also fails to eliminate the need for GCPs.

Therefore, future steps will focus on efficient ways for georeferencing areas that are to be monitored over time. Prospects for future approaches include using objects that stay consistent over time—e.g., exposed rocks—that can function as permanent GCPs. This could be achieved by painting markers on the rocks and collecting their position with a RTK DGPS. However, this method would still require extensive field campaigns for any new sites in which markers would have to be established and measured with a RTK DGPS. Also painted markers will have to be upkept to ensure they remain visible for future campaigns, and of course it will be necessary to ensure that the method used to mark the rocks does not introduce any harmful substances into the environment. Alternatively, onboard, accurate RTK GPS units and post processed kinematic (PPK) solutions are now becoming a populate and more cost-effective option of geotagging UAS imagery. It is yet to be seen if they can achieve a high absolute accuracy in a repeatable fashion and thus if they would be a viable option for creating accurate DSMs of *Sphagnum* peatlands.

4.2. Hydrological Models

The results of the hydrological modelling provide a good qualitative indication of flow accumulation in *Sphagnum* dominated peatlands and are in line with the study by Lucieer et al. [33], where the same TauDEM tools were used to simulate snowmelt in Antarctic moss beds. The topography of the study area of Lucieer et al. [33] is similar to these study sites, as they both consist of low vegetation cover and rocks, with a complex hydrological micro-topography. For the Monte Carlo simulation, a vertical error had to be defined. In reality, this error spatially varies as it is related to geometry of the camera [33]. Additionally, the accuracy assessment demonstrated the variability of the DSM vertical error between study sites and scenarios. However, as this study aimed to compare the performance of the DSM regarding the different scenarios, all other variables were kept constant.

The results from the Basin site showed that if the artificial slope present in the DSM is too large it is not possible to derive reliable hydrological maps. However, for the Heath site, the DSM generated without any ground control did not deviate significantly from the reference model, possibly because the Sky_GCP scenario contained artificial slopes (~0.35°) that were much less than the natural slope of the site (~6–7°). Small differences for the Heath site in streamlines became visible between the flow accumulation map of the GCP and Sky_GCP scenarios, which are mainly caused by the difference in size between the DSMs. The Heath reference DSM was built with photos covering a larger area than the Sky_GCP scenario. As the hydrological model input values of surface water are defined as the size of each pixel (10 cm), a DSM with a larger area results in higher accumulation values and can influence the flow direction.

This study has demonstrated the best methodology for the creation of accurate hydrological models of *Sphagnum* mires. This methodology will now be used to map and monitor the hydrology of *Sphagnum* mires in a representative selection of sites throughout the effected landscape as part of an ongoing restoration program. The ultra-high resolution DSM data is essential to detect the micro-topographic changes in the damaged mires and also to model the potential locations for restoration intervention.

The hydrological models could be further improved by including vegetation variables, such as water infiltration. However, because the *Sphagnum* sites that were visited during this study were largely damaged by fire, their water holding capacity is uncertain, hence this factor will be difficult to include. An overall objective of this project is to inform peatland rehabilitation, therefore the next step will focus on quantifying hydrological changes when artificial restoration interventions (e.g., dams) are added to the hydrological surface models with the aim to increase water availability to areas with damaged *Sphagnum*. Another approach that could be of significant importance to peatland rehabilitation, is the use of spectral signatures gained from high-resolution multispectral UAS imagery to identify different health states of *Sphagnum*, which is planned for future field campaigns.

5. Conclusions

The objective of this study was to generate reliable digital surface models (DSMs) of *Sphagnum* dominated peatlands from UAS, for the purpose of creating hydrological surface models, thereby assessing efficient ways for accurate georeferencing. This has been achieved by generating three different scenarios for five study sites in northern Tasmania. Sites Heath and Jack's Lagoon presented the lowest vertical errors. The errors of All_GCP and Four_GCP scenarios were within a range of 0.03 m and for the Sky_GCP scenarios, errors remained below 0.5 m. For these two sites, artificial slopes in the DSMs were found for the Four_GCP scenarios, however these did not exceed 0.05°. DSMs without ground control showed a strong increase in artificial slope for both sites, reaching up to around 0.8°. The DSMs from the sites Basin, Flat Valley, and Eagle Valley resulted in significantly larger vertical errors for the Four_GCP scenarios and often exceeded 10 cm. Slopes for the Sky_GCP scenarios often exceeded 1°. Additionally, the slope assessment revealed doming of the Four_GCP scenarios for sites Basin and Eagle Valley. Basin, Eagle Valley and Flat Valley differed from Heath and Jack's Lagoon by shape (elongated rectangle vs. square) and complexity of topography, where for the first three sites the trees and steep rocky ridges increased the amount of variations in the vertical axis of the DSMs.

After the DSM accuracy assessment, hydrological surface models were created for Heath and Basin, using the reference scenario with all ground control points (16–20) and the Sky_GCP scenario, where no ground control points were used. After a visual comparison with the orthophoto, the reference scenarios suggested to provide good qualitative representations of flow accumulation and topographic wetness. The artificial slope of the DSM for Heath for the Sky_GCP scenario (0.35°) was too small to cause significant changes in the hydrological models. For Basin, the Sky_GCP scenario contained an artificial slope that resulted in a false representation of water accumulation in the topographic wetness index model. The use of regularly distributed GCPs are necessary to generate a reliable topography from UAS for *Sphagnum* dominated peatlands. However, for areas where *Sphagnum* is badly damaged and further damage needs to be minimized, the use of at least four GCPs around the edges and potentially an additional GCP in the center of the area, would suffice. DSMs that are generated without any ground control method are not reliable enough to be used for hydrological surface models, hence the use of GCPs is strongly advised. Further research should demonstrate whether other approaches could be used to easily facilitate accurate georeferencing of UAS imagery.

References

1. French, B.; Hope, G.; Pryor, L.D.; Bowman, D.M. The vulnerability of peatlands in the Australian Alps. *J. Aust. Netw. Plant Conserv.* **2016**, *24*, 1–16.

2. Page, S.E.; Baird, A.J. Peatlands and Global Change: Response and Resilience. *Annu. Rev. Environ. Resour.* **2016**, *41*, 35–57. [CrossRef]

3. Williams, R.; Warwaick, P.; McDougall, K.; Mansergh, I.; Heinze, D.; Camac, J.; Nash, M.; Morgan, J.; Hoffman, A. 6. Alpine ecosystems. In *Biodiversity and Environmental Change: Monitoring, Challenges and Direction*; Lindenmayer, D., Burns, E., Thurgate, N., Lowe, A., Eds.; CSIRO Publishing: Melbourne, VIC, Australia, 2014; pp. 168–212. ISBN 0643108578.

4. Cairns, S.; Robertson, G. *2014 Survey of Feral Horses (Equus ferus caballus) in the Australian Alps*; The Australian Alps Liaison Committee: Armidale, NSW, Australia, 2015; p. 23.

5. Dunlop, M.; Brown, P.R. *Implications of Climate Change for Australia's National Reserve System: A Preliminary Assessment*; Department of Climate Change: Canberra, ACT, Australia, 2008.

6. Limpens, J.; Berendse, F.; Blodau, C.; Canadell, J.G.; Freeman, C.; Holden, J.; Roulet, N.T.; Rydin, H.; Schaepman-Strub, G. Peatlands and the carbon cycle: from local processes to global implications—A synthesis. *Biogeosciences* **2008**, *5*, 1475–1491. [CrossRef]

7. Turetsky, M.R.; Benscoter, B.; Page, S.; Rein, G.; Van Der Werf, G.R.; Watts, A. Global vulnerability of peatlands to fire and carbon loss. *Nat. Geosci.* **2015**, *8*, 11–14. [CrossRef]

8. Dieleman, C.M.; Branfireun, B.A.; Mclaughlin, J.W.; Lindo, Z. Climate change drives a shift in peatland ecosystem plant community: Implications for ecosystem function and stability. *Glob. Chang. Biol.* **2015**, *21*, 388–395. [CrossRef]

9. Hope, G.; Nanson, R.; Flett, I. Peat and Organic-Rich sediments. In *The Peat-Forming Mires of the Australian Capital Territory*; Territory and Municipal Services: Canberra, ACT, Australia, 2009; pp. 31–38.

10. Clarkson, B.; Whinam, J.; Good, R.; Watts, C. Restoration of Sphagnum and restiad peatlands in Australia and New Zealand reveals similar approaches. *Restor. Ecol.* **2017**, *25*, 301–311. [CrossRef]

11. Hope, G.S.; Whinam, J. The Peatlands of the Australasian Region. *Stapfia* **2005**, *35*, 397–434.

12. Rydin, H.; Jeglum, J. Sphagnum—The builder of boreal peatlands. In *The Biology of Peatlands*; Oxford University Press: New York, NY, USA, 2013; pp. 65–75. ISBN 978-0-19-960299-5.

13. Holz, A.; Wood, S.W.; Veblen, T.T.; Bowman, D.M.J.S. Effects of high-severity fire drove the population collapse of the subalpine Tasmanian endemic conifer Athrotaxis cupressoides. *Glob. Chang. Biol.* **2015**, *21*, 445–458. [CrossRef]

14. Read, J.; Hill, R.S. The Dynamics of Some Rainforest Associations in Tasmania. *J. Ecol.* **1988**, *76*, 558–584. [CrossRef]

15. Ogden, J. Investigations of the dendrochronology of the genus Athrotaxis D. Don (Taxodiaceae) in Tasmania. *Tree Ring Bull.* **1978**, *38*, 1–13.

16. Good, R.; Wright, G.; Whinam, J.; Hope, G. Restoration of mires of the Australian Alps following the 2003 wildfires. In *Altered Ecologies: Fire, Climate and Human Influences on Terrestrial Landscapes*; Haberle, S., Stevenson, J., Prebble, M., Eds.; ANU Press: Canberra, ACT, Australia, 2010; pp. 353–362.

17. Hope, G. The mountain mires of southern New South Wales and the Australian Capital Territory: Their history and future. In *Proceedings of an International Year of Moutains Conference*; Mackay, J., Ed.; Australian Alps Liaison Committee: Canberra, ACT, Australia, 2003; pp. 65–67.

18. Whinam, J.; Hope, G.; Good, R.; Wright, G. Post-fire experimental trials of vegetation restoration techniques in the peatlands of Namadgi (ACT) and Kosciuszko National Parks (NSW), Australia. In *Terra Australis*; ANU Press: Canberra, ACT, Australia, 2010; Volume 32, pp. 364–379.

19. Natural Values Conservation Branch. *Assessment of the Ecological Impacts of the 2016 Mersey Forest Fire Complex*; Nature Conservation Report no 17/5; Department of Primary Industries, Parks, Water and Environment: Hobart, TAS, Australia, 2017; p. 142.

20. Wimbush, D.J.; Costin, A.B. Trends in Vegetation at Kosciusko. II. Subalpine Range Transects, 1959–1978. *Aust. J. Bot.* **1979**, *27*, 789–831. [CrossRef]

21. Kirkpatrick, J.B.; Dickinson, K.J.M. The impact of fire on tasmanian alpine vegetation and soils. *Aust. J. Bot.* **1984**, *32*, 613–629. [CrossRef]

22. Harris, R.M.B.; Beaumont, L.J.; Vance, T.R.; Tozer, C.R.; Remenyi, T.A.; Perkins-Kirkpatrick, S.E.; Mitchell, P.J.; Nicotra, A.B.; McGregor, S.; Andrew, N.R.; et al. Biological responses to the press and pulse of climate trends and extreme events. *Nat. Clim. Chang.* **2018**, *8*, 579–587. [CrossRef]

23. Clarke, P.J.; Martin, A.R.H. Sphagnum peatlands of Kosciuszko National Park in relation to altitude, time and disturbance. *Aust. J. Bot.* **1999**, *47*, 519–536. [CrossRef]

24. Turner, D.; Lucieer, A.; de Jong, S.M. Time series analysis of landslide dynamics using an Unmanned Aerial Vehicle (UAV). *Remote Sens.* **2015**, *7*, 1736–1757. [CrossRef]

25. Hemerly, E.M. Automatic georeferencing of images acquired by UAV's. *Int. J. Autom. Comput.* **2014**, *11*, 347–352. [CrossRef]

26. Clapuyt, F.; Vanacker, V.; Oost, K. Van Geomorphology Reproducibility of UAV-based earth topography reconstructions based on Structure-from-Motion algorithms. *Geomorphology* **2016**, *260*, 4–15. [CrossRef]

27. Harwin, S.; Lucieer, A. Assessing the accuracy of georeferenced point clouds produced via multi-view stereopsis from Unmanned Aerial Vehicle (UAV) imagery. *Remote Sens.* **2012**, *4*, 1573–1599. [CrossRef]

28. Tonkin, T.N.; Midgley, N.G. Ground-control networks for image based surface reconstruction: An investigation of optimum survey designs using UAV derived imagery and structure-from-motion photogrammetry. *Remote Sens.* **2016**, *8*, 786. [CrossRef]

29. Harwin, S.; Lucieer, A.; Osborn, J. The impact of the calibration method on the accuracy of point clouds derived using unmanned aerial vehicle multi-view stereopsis. *Remote Sens.* **2015**, *7*, 11933–11953. [CrossRef]

30. Gindraux, S.; Boesch, R.; Farinotti, D. Accuracy assessment of digital surface models from Unmanned Aerial Vehicles' imagery on glaciers. *Remote Sens.* **2017**, *9*, 186. [CrossRef]

31. Fraser, B.T.; Congalton, R.G. Issues in Unmanned Aerial Systems (UAS) data collection of complex forest environments. *Remote Sens.* **2018**, *10*, 908. [CrossRef]

32. Verhoeven, G. Software Review Taking Computer Vision Aloft—Archaeological Three-dimensional Reconstructions from Aerial Photographs with PhotoScan. *Archaeol. Prospect.* **2011**, *73*, 67–73. [CrossRef]

33. Lucieer, A.; Turner, D.; King, D.H.; Robinson, S.A. Using an unmanned aerial vehicle (UAV) to capture micro-topography of antarctic moss beds. *Int. J. Appl. Earth Obs. Geoinf.* **2014**, *27*, 53–62. [CrossRef]

34. Tarboton, G. A new method for the determination of flow directions and upslope areas in grid digital elevation models. *Water Resour. Res.* **1997**, *33*, 309–319. [CrossRef]

35. Fairfield, J.; Leymarie, P. Drainage networks from grid digital elevation models. *Water Resour. Res.* **1991**, *27*, 709–717. [CrossRef]

36. Tarboton, D.G.; Mohammed, I.N. *TauDEM 5.1: Quick Start Guide to Using the TauDEM ArcGIS Toolbox*; Utah State University: Logan, UT, USA, 2013.

37. Beven, K.J.; Kirkby, M.J. A physically based, variable contributing area model of basin hydrology. *Hydrol. Sci.* **1979**, *24*, 43–69. [CrossRef]

38. D'Oleire-Oltmanns, S.; Marzolff, I.; Peter, K.; Ries, J. Unmanned Aerial Vehicle (UAV) for Monitoring Soil Erosion in Morocco. *Remote Sens.* **2012**, *4*, 3390–3416. [CrossRef]

39. Mancini, F.; Dubbini, M.; Gattelli, M.; Stecchi, F.; Fabbri, S.; Gabbianelli, G. Using unmanned aerial vehicles (UAV) for high-resolution reconstruction of topography: The structure from motion approach on coastal environments. *Remote Sens.* **2013**, *5*, 6880–6898. [CrossRef]

40. Uysal, M.; Toprak, A.S.; Polat, N. DEM generation with UAV Photogrammetry and accuracy analysis in Sahitler hill. *Measurement* **2015**, *73*, 539–543. [CrossRef]

41. James, M.R.; Robson, S.; Oleire-oltmanns, S.; Niethammer, U. Geomorphology Optimising UAV topographic surveys processed with structure-from-motion: Ground control quality, quantity and bundle adjustment. *Geomorphology* **2017**, *280*, 51–66. [CrossRef]